Structural, electronic, mechanical, and transport properties of phosphorene nanoribbons: Negative differential resistance behavior

Ajanta Maity, Akansha Singh,* and Prasenjit Sen†
Harish-Chandra Research Institute, HBNI, Chhatnag Road, Jhunsi, Allahabad 211019, India

Aniruddha Kibey and Anjali Kshirsagar
Center for Modeling and Simulation, Savitribai Phule Pune University, Pune 411007, India
and Department of Physics, Savitribai Phule Pune University, Pune 411007, India

Dilip G. Kanhere
Center for Modeling and Simulation, Savitribai Phule Pune University, Pune 411007, India
(Received 2 September 2015; revised manuscript received 12 July 2016; published 15 August 2016; corrected 12 June 2018)

Structural, electronic, mechanical, and transport properties of two different types of phosphorene nanoribbons are calculated within the density functional theory and nonequilibrium Green's function formalisms. Armchair nanoribbons turn out to be semiconductors at all widths considered. Zigzag nanoribbons are metallic in their layer-terminated structure, but undergo Peierls-like transition at the edges. Armchair nanoribbons have smaller Young's modulus compared to a monolayer, while zigzag nanoribbons have larger Young's modulus. Edge reconstruction further increases the Young's modulus of zigzag nanoribbons. A two-terminal device made of zigzag nanoribbons show negative differential resistance behavior that is robust with respect to edge reconstruction. We have also calculated the I-V characteristics for two nonzero gate voltages. The results show that the zigzag nanoribbons display strong p-type character.

DOI: 10.1103/PhysRevB.94.075422

I. INTRODUCTION

Since the synthesis of graphene sheets [1] there has been a steady interest in two-dimensional (2D) materials mainly for electronic applications. Graphene turned out to be a material with remarkable properties: very high charge carrier mobility ($\sim$200 000 cm^2/V s) [2], high thermal conductivity ($\sim$5000 W/mK), and unusually large mechanical strengths (Young's modulus of $\sim$2 TPa) [3]. However, the advantage of high mobility in field effect transistor (FET) devices is lost due to absence of a band gap in graphene which results in a large off-state current and a low drain current modulation.

This has led to search for other 2D materials with reasonable mobilities and sizable gaps. A class of layered transition metal dichalcogenides (TMDs), MoS_2, $MoSe_2$, WS_2, and WSe_2, have attracted a lot of attention lately [4]. Monolayers and few layers of these materials have been synthesized through mechanical and chemical exfoliation [5]. These have shown mobility values of a few hundred cm^2/V s. Drain current modulation as high as 10^8 has been achieved in FET devices made of a monolayer MoS_2 [6].

For the last couple of years, black phosphorus (BP), the most stable allotrope of phosphorus, has attracted great attention. BP is a layered material like graphite in which successive layers are held together by van der Waals (vdW) forces [7]. Few-layer samples of phosphorene (name given to a monolayer of BP) have been exfoliated by various means [8–11]. FET devices have also been made using few-layer phosphorene as the channel. Few-layer phosphorene offers a reasonable mobility and band gap. While the measured band gap of bulk BP is $\sim$0.3 eV [12–14], it increases with decreasing number of layers [9]. Mobility close to 1000 cm^2/V s has been measured in few-layer devices, and a drain current modulation of 10^5 has been achieved [8]. These properties make phosphorene an attractive material for electronic applications, and therefore a detailed quantitative understanding of its fundamental physical properties is warranted.

That there is a significant interest in phosphorene currently is evident from the number of experimental and theoretical works on its electronic and mechanical properties [15–17], thermal conductivity and thermoelectric effect [18–21], photoluminescence [22], etc. The effect of native defects [23], vacancies, and adatoms [24] have also been investigated. Tunability of electronic properties of phosphorene, for example due to strain [15,25,26], brings out interesting application potentials for this material. In addition to phosphorene sheets, phosphorene nanoribbons (PNR) have also been studied theoretically [27–30]. One of the initial motivations for studying PNRs was to have an additional control over the band gap through manipulating the width of the PNRs [27]. In any case, channel materials are finite in the direction perpendicular to the current, which gives a motivation for studying PNRs. It may be noted that it is possible to form PNRs with three different types of edges: zigzag (zPNR), rugged (or armchair) (aPNR), and linear (lPNR) edges.

Although the excitement generated by phosphorene is due to its promising role as a channel material in FETs, we are aware of only two other theoretical works on transport (I-V) characteristics of PNRs so far [31,32]. Zhang *et al.* [31] have studied transport properties of zPNR devices of width 5 unit cells and lengths ranging from 3 to 6 units cells. More importantly, they calculated transport characteristics of layer-terminated (as obtained by truncating the monolayer), zPNR

*Present address: Department of Physics, Tel-Aviv University, Tel-Aviv, Israel.
†prasen@hri.res.in

devices without considering reconstruction. As we show later, edges of zPNRs undergo structural reconstruction. Therefore, it is crucial to check whether the most important characteristic, namely negative differential resistance (NDR), reported by Zhang *et al.* survives edge reconstruction. In addition, we study transport properties of zPNR devices of larger widths and lengths. Thus our calculations are complimentary to those of Zhang *et al.* Wu *et al.* [32], on the other hand, studied transport characteristics of edge passivated zPNRs. Thus the system they explored is very different from ours. And not surprisingly, the transport pathways in these two systems are also different, as we discuss in detail in Sec. III B. Our work goes beyond these two works on two other counts. First, we report transport characteristics of an aPNR device. It may be noted that gate voltage is usual control on drain current in FETs. Therefore, we have studied the effects of gate voltage on transport in zPNR.

The rest of the paper is organized as follows. In Sec. II we discuss the theoretical methods employed to calculate the structural, electronic, and transport properties of monolayer phosphorene and PNRs. In different subsections of Sec. III we present our findings on the structural, electronic, and transport properties of PNRs. We draw our conclusions in Sec. IV.

II. METHODS

The geometry and electronic structure calculations for phosphorene sheet and PNRs are performed within a plane wave density functional theory (DFT) formalism. An energy cutoff of 500 eV is used for the plane wave basis set. Interactions between the valence electrons and the ion cores are represented by projector augmented wave (PAW) potentials. The PBE gradient corrected functional [33] is used for the exchange-correlation energy. In a few cases we have also employed the hybrid HSE06 functional proposed by Hyde, Scuseria, and Ernzerhof [34,35] to have a more accurate estimate of the band gap. We could not use it in all the cases because of its significant computational cost compared to the PBE functional. In the HSE06 functional the short-range part of exchange is a mix of Hartree-Fock (HF) nonlocal and PBE semilocal functionals. The long-range parts of exchange and correlation are taken exactly as in PBE. The full exchange-correlation functional in HSE06 is written as

$$E_{xc}^{\mathrm{HSE}} = eE_x^{\mathrm{HF,SR}}(\omega) + (1-e)E_x^{\mathrm{PBE,SR}}(\omega) + E_x^{\mathrm{PBE,LR}}(\omega) + E_c^{\mathrm{PBE}}, \quad (1)$$

where $E_x^{\mathrm{HF,SR}}$, $E_x^{\mathrm{PBE,SR}}$, and $E_x^{\mathrm{PBE,LR}}$ are the short- and long-range parts of the HF and PBE exchange energies, respectively. E_c^{PBE} is the PBE correlation energy. ω gives the inverse length that separates short- and long-range Coulomb interactions. e determines the fraction of short-range HF exchange. We used $e = 0.25$ and $\omega = 0.2$ Å^{-1}, the default values in HSE06. Use of HSE06 increases the band gap compared to PBE, as expected. An $(8 \times 8 \times 1)$ Mokhorst-Pack (MP) k-point mesh is used for Brillouin zone (BZ) integration for electronic structure calculations of the monolayer. For the nanoribbons running along the x and y directions (defined below) $(8 \times 1 \times 1)$ and $(1 \times 8 \times 1)$ MP k-point meshes were employed. We kept a vacuum space of 15 Å in all the nonperiodic directions in the supercell. All the atoms in the supercells were relaxed using a conjugate gradient method till all the force components became less than 0.01 eV/Å. The VASP code [36–39] was used for these calculations.

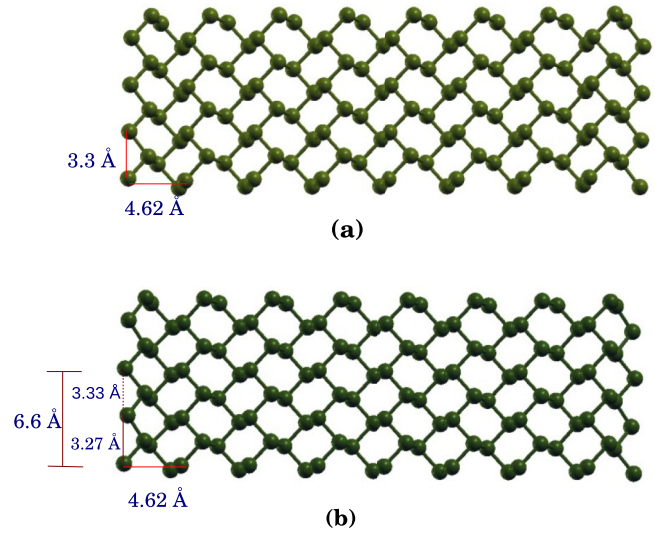

FIG. 1. (a) Structure of monolayer phosphorene and (b) structure of edge reconstructed zPNR (see text for details). Lattice constants in the two in-plane directions are shown.

A phosphorene monolayer has a rectangular unit cell with four atoms forming the basis. Atomic structure of phosphorene layer is shown in Fig. 1(a). The direction along the trenches is designated as y in this work, while the perpendicular direction in the plane of the monolayer is designated as x. The direction perpendicular to the monolayer plane is designated as z. The optimum lattice constants of a monolayer along the x and y directions are found to be 4.62 and 3.3 Å, respectively, in good agreement with other DFT calculations [40].

It is important to note the differences between monolayers of graphene and phosphorene. A graphene layer is atomically flat and each C atom is sp^2 hybridized forming σ bonds with three in-plane neighbors. A phosphorene monolayer, however, is puckered with the P atoms being sp^3 hybridized. Each of them is covalently bonded to three neighbors, and has one lone pair of electrons in the fourth hybrid orbital [41]. One may have two different types of edges for PNRs that are periodic along y: edges with P atoms that are either onefold or twofold coordinated [27]. Earlier we termed these as the lPNR and zPNR, respectively. In case of PNR's periodic along x, only one type of edge is possible in which, of the four atoms at one edge of the unit cell, two are twofold coordinated and the other two are threefold coordinated. These have been called the rugged edges or armchair edges, and these PNRs the aPNR.

The transport calculations are performed within the nonequilibrium Green's functions (NEGF) formalism implemented in the Quantumwise Virtual Nanolab [42–45]. We used double-zeta polarized basis sets with a mesh cutoff of 70 Ry to represent the electronic wave functions. The electron temperature was set at 300 K. We used the same gradient corrected PBE functional for the exchange-correlation energy. For BZ integrations in these calculations, 100 k points were used in the direction of current. Such a large number of k points was

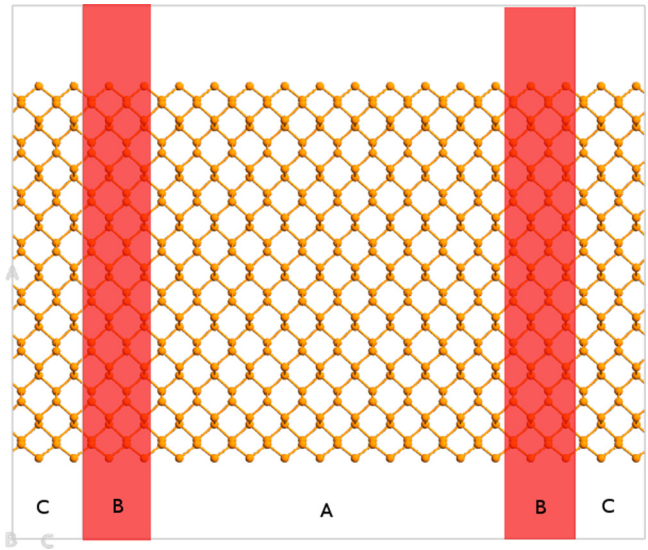

FIG. 2. Top view of the geometry of two-terminal zPNR device.

needed for convergence when simulating semi-infinite leads. We consider a two-terminal device. The essential geometry of our two-terminal device for a zPNR is shown in Fig. 2. The region marked "A" (scattering region) is a finite piece of zPNR whose transport properties are calculated. The regions marked "C" on the two extremes of the device are the semi-infinite electrodes. These are relaxed, edge reconstructed zPNRs. Once optimized, electron densities in these regions are held fixed during the transport calculations. The regions marked "B" are called the electrode extensions. These act as transition regions between the finite scattering region A and the semi-infinite electrodes C, and are allowed to relax both structurally and electronically during the transport calculations. The width of region B is so chosen that the basis sets from regions A and C do not overlap. Due to this the density in region C is the same as that of the bulk charge density for zPNR. To calculate the electronic structure and transmission function of the device Poisson's equation is solved in region B-A-B in a self-consistent manner. The boundary condition is given by the continuity of the charge density at the interface of regions B and C. For a given bias voltage V, the Green's function for the device at an energy E is given by

$$G_D(E) = [ES_D - H_D - \Sigma_L(E) - \Sigma_R(E)]^{-1}, \quad (2)$$

where S_D is the overlap matrix in the device, H_D is the Hamiltonian for the device (scattering region), and Σ_L and Σ_R are the self-energy matrices describing the coupling of the scattering region to the left and right electrodes, respectively. The broadening matrices are given by $\Gamma_L = i(\Sigma_L - \Sigma_L^\dagger)$ and $\Gamma_R = i(\Sigma_R - \Sigma_R^\dagger)$.

The quantity of utmost importance in the Landauer-Büttiker formalism is the transmission coefficient which is the trace of the transmission matrix. The transmission matrix is given by

$$T(E) = \mathrm{Tr}[\Gamma_L(E)G_D(E)\Gamma_R(E)G_D^\dagger(E)]. \quad (3)$$

The transmission matrix can also be written as

$$T_{nm}(E) = \sum_k t_{nk}^\dagger t_{km}, \quad (4)$$

where t_{nk} is the transmission amplitude from the kth Bloch state in the source electrode to the nth Bloch state in the drain electrode. And the transmission coefficient

$$T(E) = \mathrm{Tr}[T_{ij}(E)]. \quad (5)$$

The current pathways in the device can be understood from the spatial profile of the transmission eigenstates which are linear combination of the Bloch states $\sum_n e_{\alpha,n}\psi_n$, where the vectors $e_{\alpha,n}$ diagonalize the transmission matrix

$$\sum_m T_{nm}e_{\alpha,m} = \lambda_\alpha e_{\alpha,n},$$

with transmission eigenvalue λ_α. Once the transmission function is obtained, the current was calculated using the standard Landauer-Büttiker formalism with

$$I = \frac{2e}{\hbar}\int_{-eV/2}^{eV/2} T(E,V)[f_L(E-\mu_L) - f_R(E-\mu_R)]dE, \quad (6)$$

where f is the Fermi distribution function, $T(E,V)$ is the transmission function at a given energy E for a bias voltage V. $T(E,V)$ becomes a function of V because the DOS of the electrodes change under application of bias voltage. Exactly the same level of theory has been used in Refs. [31,32] allowing a direct comparison of the results.

III. RESULTS AND DISCUSSION

A. Geometry and electronic structure of PNRs

A phosphorene monolayer is found to have a direct gap of 0.9 eV in PBE. The CBM occurs exactly at the Γ point in the Brillouin zone. The VBM occurs marginally away from the Γ point towards Y. Therefore, a monolayer phosphorene can be considered practically to have a direct gap. This finding is in agreement with what has been reported by Sa *et al.* [46] and Tran *et al.* [47]. Using HSE06 also, the VBM was found slightly away from the Γ point, while the CBM was still at the Γ point. The gap turned out to be 1.6 eV. These results are in very good agreement with the results published earlier [8,40].

As we stated before, one can form three different types of PNRs. Energetic stability of PNRs are determined by their formation energies. Formation energy (FE) of a PNR is defined as

$$\mathrm{FE} = E_\mathrm{T} - n\mu_\mathrm{P}, \quad (7)$$

where E_T is the total energy of the PNR composed of n phosphorus atoms, and μ_P is the chemical potential of a P atom in its reference state. In these calculations we have taken a phosphorene monolayer as the reference state. The larger the FE, the more energetically unfavorable is a structure. In their layer-terminated structures, the formation energies of the lPNRs turn out to be 1.2 eV per edge atom, while that of zPNRs is 0.67 eV per edge atom. The formation energy of the aPNRs is much smaller, 0.31 eV per edge atom. These numbers are consistent with the fact that lPNRs have the largest number of dangling bonds per edge atom, two. zPNRs, on the other hand, have one dangling bond per edge atom, and hence have a smaller formation energy. aPNRs have, on average, 1/2 dangling bond per edge atom. Consequently, it has the smallest

TABLE I. Lattice constants and calculated band gaps of aPNRs of various widths.

Width	Lattice constant (Å)	Band gap (eV)
2	5.07	1.20
3	4.75	1.03
4	4.69	0.70
5	4.67	0.53
6	4.66	0.48
8	4.65	0.42
10	4.64	0.42

FE. Here we will consider only the aPNRs and the zPNRs. The lPNRs have the highest formation energies, and their edges are highly unstable undergoing large reconstructions. Therefore, they will not be considered here. Details about geometry and electronic structure of lPNRs can be found in Ref. [27].

We optimized the lattice constants of aPNRs and zPNRs in the periodic directions, should they be different from the lattice constants of the monolayer in the corresponding directions. The lattice constant of zPNRs turned out to be the same as that of a monolayer, i.e., 3.3 Å, for all widths. Lattice constant of aPNRs, however, depends strongly on the width, particularly at smaller widths. It is found to be 5.07 Å for an aPNR of width 2. It decreases with increasing width, being 4.75 Å at width 3, and 4.69 Å at width 4. After that the decrease is gradual, being 4.65 Å at a width of 8 unit cells. Lattice constant of all aPNRs studied here are reported in Table I.

aPNR: Having optimized their lattice constants, we studied electronic properties aPNRs of width 2–10 unit cells. All these turn out to be indirect band gap semiconductors (in PBE). For aPNRs of widths 4–6, the VBM appears at the Γ point and the CBM appears between the Γ and the zone boundary. The band gap of aPNRs of width 2 and 3 are 1.20 and 1.03 eV, respectively, larger than the gap of a monolayer. The band gap decreases monotonically with increasing width. At width 4, it falls below the gap of a monolayer, and is 0.70 eV. Calculated band gaps of all the aPNRs are given in Table I. Guo *et al.* [48] have studied these nanoribbons of width 7–12 unit cells and have found them to be indirect gap semiconductors. Carvalho *et al.* [28] have also reported similar calculations. We calculated a ribbon of width 10, and this also turned out to be a semiconductor having an indirect gap of 0.42 eV in agreement with the results in Ref. [48]. One may conclude that the band gap of aPNRs is not very sensitive to the width beyond 6 unit cells, and an indirect to direct gap transition occurs somewhere between a ribbon of width 12 unit cells and the monolayer. Band structure of an aPNR of width 8 is shown in Fig. 3.

zPNR: In contrast to the aPNRs, the zPNRs have metallic band structure at all widths between 1–8 in their layer-terminated structures. In all of these, two bands cross the Fermi energy. In zPNRs of width larger than 3 unit cells, both these bands are exactly half-filled. This is understandable because there is only one dangling bond per edge atom in the zPNRs. The band structure turns out to be different for widths 1–3. The k points at which these bands cross the Fermi energy depend on the width of the PNR. However, none of these crossings happens at simple fractions such a 1/2 or 1/4 from Γ to the

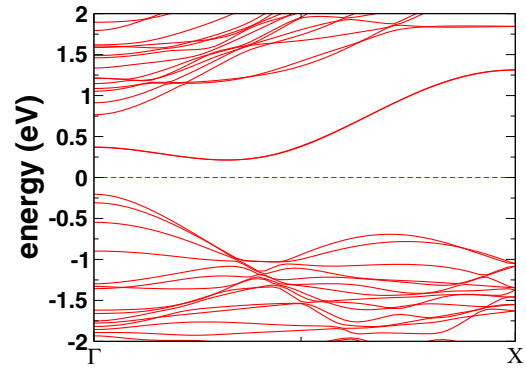

FIG. 3. Band structure plot of an 8 unit cell wide aPNR.

zone boundary. We focus on zPNRs of width 4 and more as these are likely to be practically important. Band structure and the density of states (DOS) of a layer-terminated zPNR of width 8 is shown in Fig. 4(a). The bands crossing the Fermi energy are formed of the p_x and p_z orbitals of the edge atoms, and interestingly, both the bands have contributions from P atoms at both edges. Therefore the metallic nature is due to the one-dimensional (1D) chain of P atoms at the two edges.

The half-filled bands due to the 1D chain of edge atoms present an unstable situation. It is well known that such 1D metallic systems undergo structural distortion through dimerization of successive atom pairs. The consequent doubling of the unit cell halves the BZ, leading to the opening of a small gap at the new zone boundary. This phenomenon, proposed by Peierls [49], is known as Peierls transition. To find out if the edges of zPNRs indeed undergo such a Peierls transition, we performed calculations with a supercell consisting of two primitive unit cells along the length of the zPNR. After relaxation, two successive atoms along the edges were indeed found to dimerize. In particular, the distance between successive atoms in the periodic direction along the

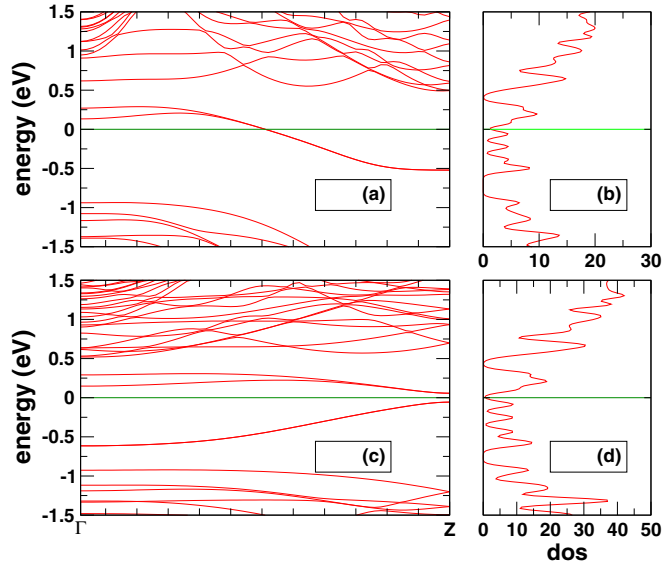

FIG. 4. Band structure plots of an 8 unit cell wide zPNR for (a) layer-terminated structure and (c) structure after edge reconstruction. (b) and (d) depict the corresponding DOS.

TABLE II. Energy gain (meV/edge dimer) and gap value (eV) for edge reconstructed zPNRs of different widths.

Width	Energy gain	Gap
4	9.8	0.11
5	8.4	0.14
6	11.0	0.12
7	13.0	0.14
8	10.0	0.11

first few rows of atoms (first, second, and third for width 8) starting from the edges decreases marginally to 3.27 Å from 3.3 Å in the layer-terminated structure. For other atomic rows in the interior of the PNR, the atoms have a separation of 3.3 Å, as in a monolayer. Structure of such an edge reconstructed zPNR is shown in Fig. 1(b). This small distortion decreases the total energy of a zPNR, and also opens a gap. The exact value of energy gain and gap depends on the width for the PNR. These values for zPNRs of width from 4 up to 8 unit cells are given in Table II. The energy gain and gap values are nearly the same for all widths in this range. Band structure and DOS of a zPNR of width 8 after gap opening is shown in Figs. 4(c) and 4(d). If this phenomenon of gap opening is indeed a Peierls transition, one expects the atomic character of the VBM and the CBM after gap opening to be the same as the character of the edge bands crossing the Fermi energy in the layer-terminated metallic nanoribbons. Indeed, the VBM at the zone boundary is formed of the p_x and p_z orbitals of the edge atoms in the edge reconstructed PNR. The CBM has contributions from some of the interior atoms in addition to dominant contribution from the edge atoms. The charge density originating from the half-filled bands before reconstruction, and the VBM and CBM after reconstruction are shown in Fig. 5. It is obvious that these bands are localized along the two edges.

Also important are the mechanical properties of PNRs vis-a-vis the monolayer, and the effect of edge reconstruction on properties of zPNRs. Monolayer and few-layer phosphorene have superior mechanical properties compared to such hard material as cast iron whose Young's modulus is 110 GPa. Wei *et al.* [17] found a monolayer phosphorene to have a Young's modulus of 166 GPa along the zigzag direction. Young's modulus decreases with the number of layers, but is still quite large (159 GPa) for four-layer black phosphorus. It is more natural to express the Young's modulus of a 2D sheet in units of J/m^2. We found the Young's modulus for a monolayer phosphorene along the zigzag and armchair directions to be 91.8 and 29.5 J/m^2, respectively. These are in good agreement with what Qiao *et al.* [40] reported, 101.6 and 28.9 J/m^2, respectively. Thus the structure of a phosphorene layer is much softer along the armchair direction. Creating a PNR along the armchair direction makes the structure even softer. The Young's modulus of an aPNR of width 8 is found to be 18.5 J/m^2. In contrast to this, PNR in the zigzag direction is a little harder than the monolayer. An edge-terminated zPNR of width 8 has a Young's modulus of 97.9 J/m^2. Edge reconstruction increases its hardness slightly due to the formation of new bonds at the edges. The Young's modulus of the edge reconstructed zPNR turns out to be 98.1 J/m^2. Thus applications that rely on superior mechanical properties of phosphorene layers can take further advantage by using zPNRs rather than monolayers.

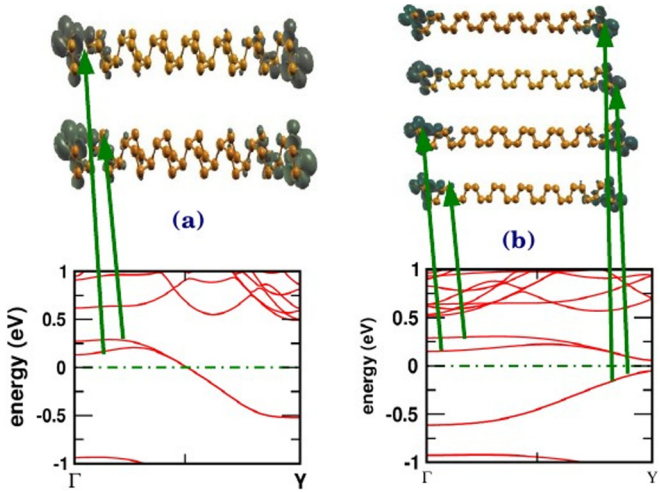

FIG. 5. Isosurfaces of charge density from (a) the half-filled bands in the layer-terminated and (b) VBM and CBM of edge reconstructed zPNR. These figures show that the charge density is localized at the edges.

B. Transport properties of PNRs

Now we present results of our transport calculations of aPNRs and zPNRs using the NEGF formalism as described earlier. Further details on the method can be found in Refs. [44,45]. The device geometry for zPNR is described earlier. A similar geometry is used for a two-terminal aPNR device. In our zPNR device, the length of the scattering region A is 33 Å, while that of each of the B and C regions is 5.75 Å. Similarly for the aPNR device the length of the scattering region A is 36.96 Å, while that of each of the B and C regions is 9.24 Å.

aPNR device: The *I-V* characteristics of an aPNR device is shown in Fig. 6(a). The current is negligible till a bias voltage of 0.75 eV. After this it increases rapidly. This is what

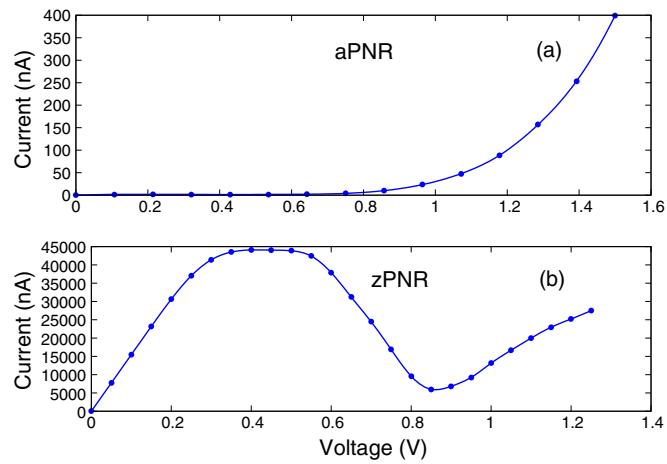

FIG. 6. *I-V* characteristics of (a) an aPNR device and (b) a zPNR device.

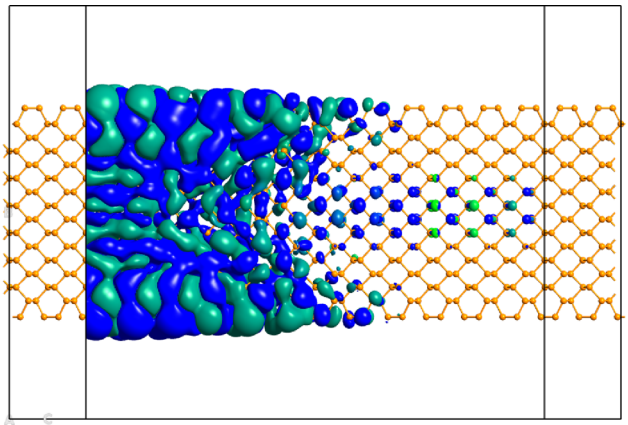

(a)

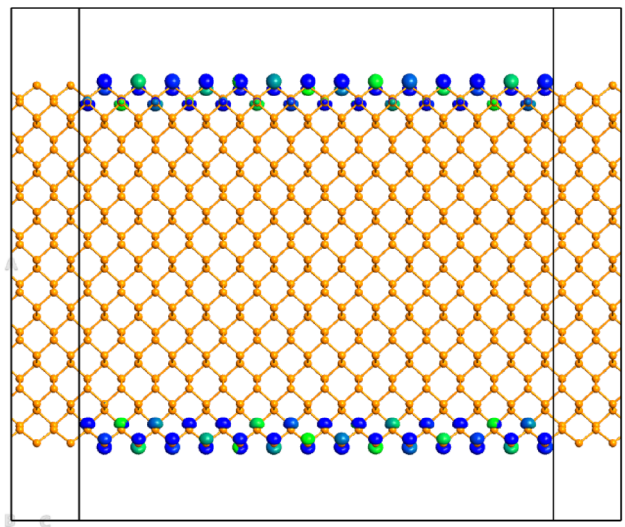

(b)

FIG. 7. Isosurface plots for transmission eigenstates for (a) aPNR device at the Fermi energy at a bias voltage of 1.25 V and (b) zPNR device at the Fermi energy at a bias voltage of 0.45 V.

one would expect in a semiconductor with sizable band gap. However, the total current is only of the order of a few hundred nano-Amperes (nA), about two orders of magnitude smaller than the current through a zPNR device at the same bias voltage (discussed below). An important question is the path through which the current flows in the channel material. We have traced the pathway for the current by studying the eigenvectors of the transmission matrix. Figure 7(a) shows an isosurface plot of such an eigenvector at the Fermi energy of the device for a bias voltage of 1.25 V. The transmission eigenstate has large amplitude near the left electrode. The amplitude decreases as we move from the left electrode to the right. Near the right electrode the amplitude nearly vanishes giving a small current.

zPNR device: Next we studied I-V characteristics of a zPNR device, and this turns out to be more interesting. The calculated I-V curve for this device in absence of a gate voltage is shown in Fig. 6(b). Clearly it shows a NDR behavior. Initially, the current increases almost linearly with the applied bias voltage, and shows saturation at ∼0.35 V. Thereafter the current remains nearly constant till ∼0.5 V forming a small plateau. With further increase in bias voltage, the current starts decreasing and reaches a minimum at ∼0.85 V. Beyond this, increase in bias increases the current again. This trend is maintained till ∼1.25 V. A comparison with the results of Zhang *et al.* [31] is in order here. As already pointed out, they studied zPNR devices of different lengths and widths. The D_{54} system (width of 5, and length of 4 units cells in respective directions) studied in their work is the closest to our system in terms of size. This system also showed a peak in current at a bias voltage of ∼0.3 V, beyond which the current started decreasing. A minimum in current was obtained at ∼0.8 V. For further increase in voltage, the current showed a second, smaller peak at ∼1.0 V decreasing again beyond this. A few important points are to be noted here. First, the plateau in I-V we obtained between 0.35–0.5 V is not seen in Ref. [31]. Second, we have not seen a second peak in current followed by another NDR behavior. Thus interestingly and crucially, the NDR behavior survives edge reconstruction in the zPNR device, but the details of I-V characteristics are slightly different between the unreconstructed and reconstructed systems.

We now try to understand the NDR of the zPNR device in terms of the electronic structure of the device. One of the ways NDR has been explained in such devices is the match and mismatch of the DOS of the two leads and the positions of the HOMO and LUMO of the finite scattering region, as the bias voltage is changed [31,50,51]. The same mechanism can well explain the calculated I-V characteristics of our two-terminal zPNR device, albeit with a slight difference. The finite scattering regions of the devices in the three works just cited had finite HOMO-LUMO gaps. Though the gap in the finite sized zPNR scattering region is finite, it is small (∼0.01 eV). The DOS of the scattering region is effectively finite at the "Fermi energy," and the metallic behavior of the unreconstructed zPNR is recovered. This leads to a similarity in behavior of the devices studied in Ref. [31] and this work.

At zero bias voltage, of course, both the electrodes have exactly the same DOS, and hence the transmission function is large wherever the electrodes have electronic states. However, since the bias window is zero, there is no current. With applied bias voltage the chemical potentials in the two electrodes change. Because the device and the electrodes are symmetric, bias in the two opposite directions are equivalent. We arbitrarily define a voltage applied from left to right as positive. Under a positive bias voltage V, the chemical potential of the left (right) electrode shifts by $eV/2$ ($-eV/2$). Therefore, the DOS of the left (right) electrode shifts towards higher (lower) energies by $eV/2$. Consequently, resonance states appear and disappear within the bias window leading to nonmonotonic variation of current with bias voltage. Details of the shift in the DOS of the leads, and the consequent changes of the transmission function, are shown at a few representative bias voltages in Fig. 8. We point out the major observations in the following paragraph.

As the voltage is increased from zero up to 0.2 V, the behavior of $T(E,V)$ is as follows. The DOS of the electrodes is rather flat in the bias range as seen in Fig. 8(a). This results in a constant $T(E,V)$. Since the energy window of transmission increases linearly with increasing bias voltage, the current increases linearly. This trend continues till 0.3 V. As the voltage is increased further, the energy window for

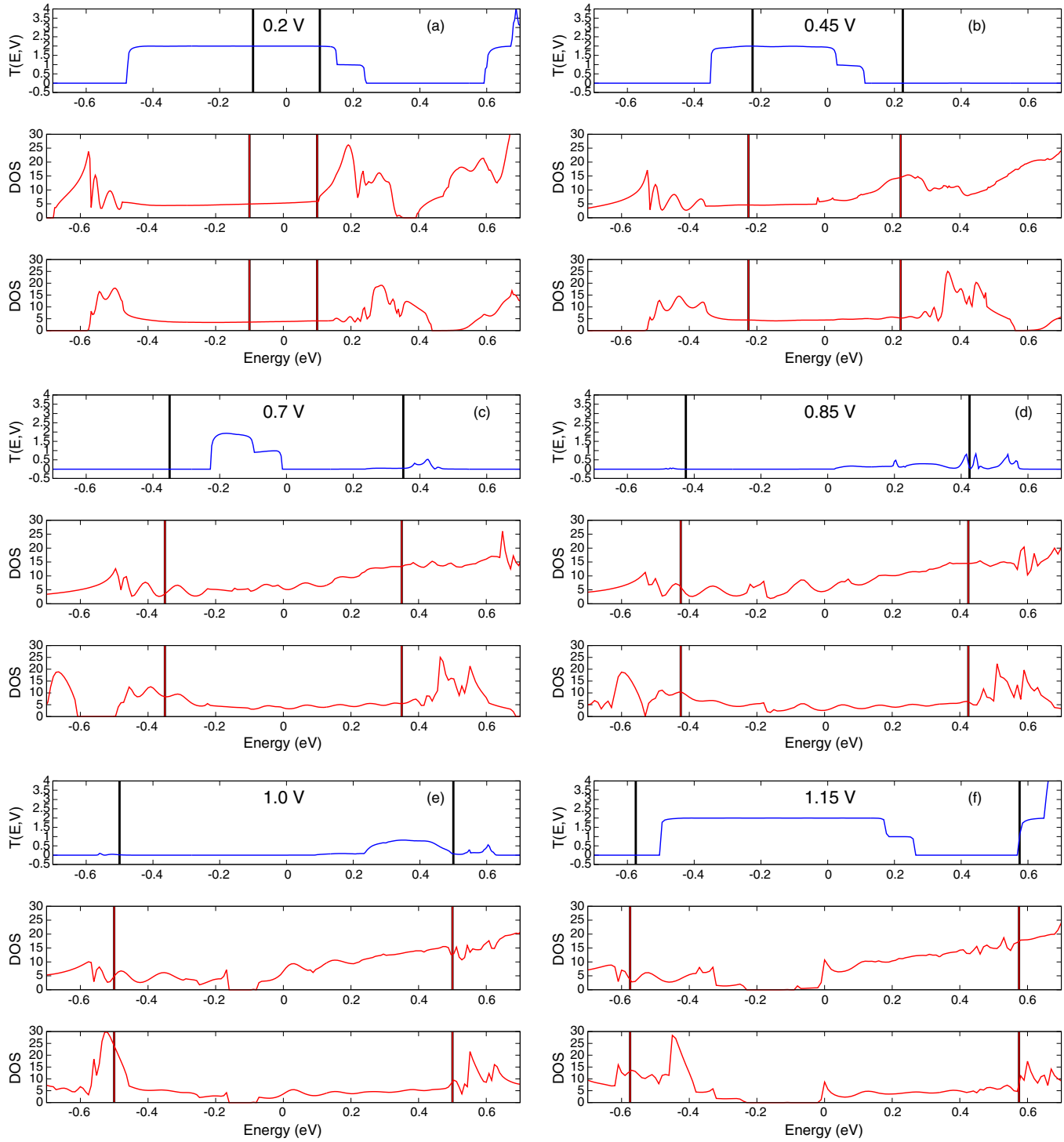

FIG. 8. Densities of states in the two electrodes, and the transmission function $T(E,V)$ at a few representative bias voltages for the two-terminal zPNR device.

transmission increases, the peak value of $T(E,V)$ remains unchanged, but its value becomes small over some parts of the energy window [Fig. 8(b)]. A balance between increasing bias window and decreasing value of $T(E,V)$ keeps the current constant over the bias range 0.35–0.5 V giving the plateau. For increase of bias beyond 0.5 V, the peak value of $T(E,V)$ and also the energy range over which nonzero $T(E,V)$ occurs decrease. This leads to a decrease in current. This is evident in Fig. 8(c). By the time the voltage increases to 0.85 V, there is only a small peak in $T(E,V)$ at ∼0.2 V while it is very small at all other energies within the bias window. This leads to a minimum of the current at this voltage [Fig. 8(d)]. The ratio of the peak and valley currents (PVR) is found to be ∼7.4. While this is small compared to PVR values of 50–200 in undefected armchair graphene nanoribbon based devices [50], or ∼4000 in defected graphene nanoribbon based devices [51],

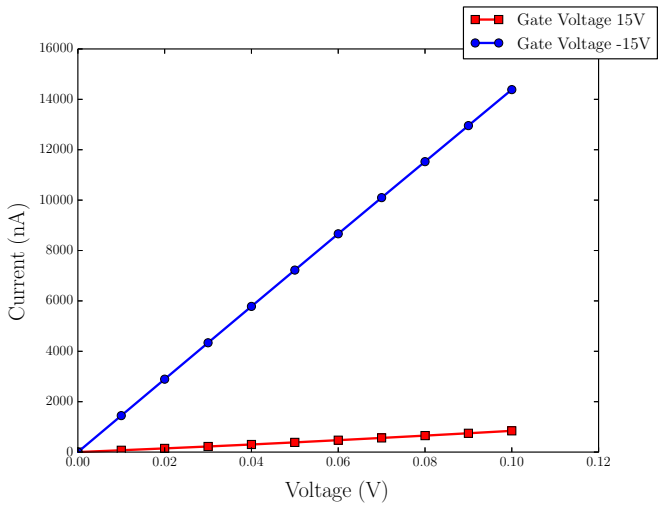

FIG. 9. I-V characteristics of zPNR device at finite gate voltages of $+15$ and -15 V.

still the existence of an NDR behavior in the new material is of interest. Moreover, it is possible that with different electrodes, and particularly two dissimilar electrodes as in Ref. [51], one may get larger values of PVR. When the bias voltage increases further, $T(E,V)$ becomes larger over a greater energy range. This can be seen in Figs. 8(e) and 8(f). This leads to an increase in current with voltage.

We have traced the pathway for current in the zPNR device also. The transmission eigenstate at a bias voltage 0.45 V at the Fermi energy is shown in Fig. 7(b). The amplitude is large only at the two edges. Thus it is clear that the current is carried by the edge states, and there is virtually no current in the central region. This is in striking contrast to the hydrogenated PNRs studied by Wu *et al.* [32] in which current is carried by the interior of the PNR. As the H-P bonds are much stronger than P-P bonds, the edge states in the hydrogenated PNRs are shifted to energies deep within the bulk bands, and the current is carried by states originating in the interior. In the edge reconstructed zPNR, the VBM and CBM still arise from the edge atoms, as we have already shown, and hence the current flows primarily through the edges.

Now we study effects of gate voltage on the conduction properties of our two-terminal device. Gate voltage is the standard way of regulating the carrier density and drain current in FETs. Experiments have found that phosphorene FETs show n-type, p-type, or ambipolar behavior for different thicknesses and different metal electrodes [52,53]. We do not have metal electrodes in this study, ruling out possibilities of barriers at the interface. So our aim is to explore and understand how and whether at all drain current may be controlled by applying gate voltages in our model device. The gate voltage was simulated in our calculations by placing the zPNR device on a dielectric material which itself rested on a gate electrode. A desired voltage can be applied to the gate electrode. We used two values, ± 15 V, in our calculations. For simplicity we took the dielectric constant of the material separating the zPNR and the gate electrode as 1. Figure 9 shows the I-V characteristics of the device with gate voltages. Note that we have been able to go only up to a bias voltage of 0.1 V, which is within the linear regime of the I-V characteristics. We could not go to higher voltages as voltages beyond 0.1 V caused convergence problems in our calculations. Even within this limited range of bias voltages, the difference between positive and negative gate voltages is obvious. The current at gate voltage of -15 V is much larger than the current at 15 V. In fact, at the bias voltage of 0.1 V, the current is an order of magnitude larger for negative gate voltage. This clearly shows the p-type behavior of the PNR in our two-terminal device.

IV. CONCLUSIONS

We have studied structural, mechanical, and electronic properties of aPNR and the zPNR. In addition, we have studied transport properties of two terminal devices formed by these two types of PNRs. aPNRs are found to be semiconducting at all widths. zPNRs are metallic in their layer-terminated structures, but undergo Peierls transition at the edges which opens a small gap in the spectrum. Because aPNRs are semiconducting, they carry almost no current for small applied voltages. Beyond a bias voltage of $\sim$0.75 V, a breakdown occurs and the current increases sharply. However, it is still much smaller than that through a zPNR device. zPNR devices show NDR behavior. It is crucial to point out that NDR in zPNRs is robust enough to survive edge reconstruction. Although the PVR values in this device is smaller compared to some other devices reported in the literature, nevertheless, existence of this phenomenon in the new material is exciting. We also found that zPNR acts as a p-type material. Young's modulus of zPNR is larger than that of a monolayer phosphorene in the same direction, while that of an aPNR is much smaller. Young's modulus of a zPNR further increases marginally after edge reconstruction. We hope these fundamental understandings of various aspects of the new material will be useful in its application.

ACKNOWLEDGMENTS

VASP calculations were performed at the cluster computing facility in HRI (www.hri.res.in/cluster/). Transport calculations are performed at the Centre for Modeling and Simulation, Savitribai Phule Pune University (SPPU), and the authors would like to acknowledge the support through DST PURSE grant to SPPU. A. Kibey and A. Kshirsagar acknowledge the financial support through a major research project funded by Nanomission initiative of Department of Science & Technology, Government of India, New Delhi.

[1] K. S. Novoselov, A. K. Geim, S. V. Morozov, D. Jiang, Y. Zhang, S. V. Dubonos, I. V. Grigorieva, and A. A. Firsov, Science **306**, 666 (2004).

[2] K. Bolotin, K. Sikes, Z. Jiang, M. Klima, G. Fudenberg, J. Hone, P. Kim, and H. Stormer, Solid State Commun. **146**, 351 (2008).

[3] J.-U. Lee, D. Yoon, and H. Cheong, Nano Lett. **12**, 4444 (2012).

[4] M. Chhowalla, H. S. Shin, G. Eda, L.-J. Li, K. P. Loh, and H. Zhang, Nat. Chem. **5**, 263 (2013).
[5] Q. H. Wang, K. Kalantar-Zadeh, A. Kis, J. N. Coleman, and M. S. Strano, Nat. Nanotech. **7**, 699 (2012).
[6] B. Radisavljevic, A. Radenovic, J. Brivio, V. Giacometti, and A. Kis, Nat. Nanotech. **6**, 147 (2011).
[7] S. Appalakondaiah, G. Vaitheeswaran, S. Lebègue, N. E. Christensen, and A. Svane, Phys. Rev. B **86**, 035105 (2012).
[8] L. Li, Y. Yu, G. J. Ye, Q. Ge, X. Ou, H. Wu, D. Feng, X. H. Chen, and Y. Zhang, Nat. Nanotechnol. **9**, 372 (2014).
[9] H. Liu, A. T. Neal, Z. Zhu, Z. Luo, X. Xu, D. Tománek, and P. D. Ye, ACS Nano **8**, 4033 (2014).
[10] A. Castellanos-Gomez, L. Vicarelli, E. Prada, J. O. island, K. L. Narsimha-Acharya, S. I. Blanter, D. J. Grönedijk, M. Buscema, G. A. Steele, J. V. Alvarez, H. W. Zandbergen, J. J. Palacios, and H. S. J. van der Zant, 2D Mater. **1**, 025001 (2014).
[11] M. Buscema, D. J. Grönedijk, S. I. Blanter, G. A. Steele, H. S. J. van der Zant, and A. Castellanos-Gomez, Nano Lett. **14**, 3347 (2014).
[12] D. Warschauer, J Appl. Phys. **34**, 1853 (1963).
[13] Y. Akahama, S. Endo, and S. Narita, J. Phys. Soc. Jpn. **52**, 2148 (1983).
[14] Y. Maruyama, S. Suzuki, K. Kobayashi, and S. Tanuma, Physica B+C **105**, 99 (1981).
[15] X. Peng, Q. Wei, and A. Copple, Phys. Rev. B **90**, 085402 (2014).
[16] P. Li and I. Appelbaum, Phys. Rev. B **90**, 115439 (2014).
[17] Q. Wei and X. Peng, Appl. Phys. Lett. **104**, 251915 (2014).
[18] L. Zhu, G. Zhang, and B. Li, Phys. Rev. B **90**, 214302 (2014).
[19] T.-H. Liu and C.-C. Chang, Nano Scale **7**, 10648 (2015).
[20] J.-W. Jiang, Nanotech **26**, 055701 (2015).
[21] S. Konabe and T. Yamamoto, App. Phys. Exp. **8**, 015202 (2015).
[22] S. Zhang, J. Yang, R. Xu, F. Wang, W. Li, M. Ghufran, Y.-W. Zhang, Z. Yu, G. Zhang, Q. Qin, and Y. Lu, ACS Nano **8**, 9590 (2014).
[23] V. Wang, Y. Kawazoe, and W. T. Geng, Phys. Rev. B **91**, 045433 (2015).
[24] P. Srivastava, K. P. S. S. Hembram, H. Mizuseki, K.-R. Lee, S. S. Han, and S. Kim, J. Phys. Chem. C **119**, 6530 (2015).
[25] M. Elahi, K. Khaliji, S. M. Tabatabaei, M. Pourfath, and R. Asgari, Phys. Rev. B **91**, 115412 (2015).
[26] J.-W. Jiang and H. S. Park, Phys. Rev. B **91**, 235118 (2015).
[27] A. Maity, A. Singh, and P. Sen, arXiv:1404.2469.
[28] A. Carvalho, A. S. Rodin, and A. H. C. Neto, Europhys. Lett. **108**, 47005 (2014).
[29] J. Xie, M. S. Si, D. Z. Yang, Z. Y. Zhang, and D. S. Xue, J. App. Phys. **116**, 073704 (2014).
[30] J. Zhang, H. J. Liu, L. Cheng, J. Wei, J. H. Liang, D. D. Fan, J. Shi, X. F. Tang, and Q. J. Zhang, Sci. Rep. **4**, 6452 (2014).
[31] C. Zhang, G. Xiang, M. Lan, Z. Tang, L. Dengab, and X. Zhang, RSC Adv. **5**, 40358 (2015).
[32] Q. Wu, L. Shen, M. Yang, Y. Cai, Z. Huang, and Y. P. Feng, Phys. Rev. B **92**, 035436 (2015).
[33] J. P. Perdew, K. Burke, and M. Ernzerhof, Phys. Rev. Lett. **77**, 3865 (1996).
[34] J. Heyd, G. E. Scuseria, and M. Ernzerhof, J. Chem. Phys. **118**, 8207 (2003).
[35] J. Heyd and G. E. Scuseria, J. Chem. Phys. **120**, 7274 (2004).
[36] G. Kresse and J. Hafner, Phys. Rev. B **47**, 558 (1993).
[37] G. Kresse and J. Hafner, Phys. Rev. B **49**, 14251 (1994).
[38] G. Kresse and J. Furthmüller, Comput. Mater. Sci. **6**, 15 (1996).
[39] G. Kresse and J. Furthmüller, Phys. Rev. B **54**, 11169 (1996).
[40] J. Qiao, X. Kong, Z.-X. Hu, F. Yang, and W. Ji, Nat. Commun. **5**, 4475 (2015).
[41] A. S. Rodin, A. Carvalho, and A. H. Castro Neto, Phys. Rev. Lett. **112**, 176801 (2014).
[42] Atomistix toolkit version 13.8, quantumwise a/s (2015).
[43] Virtual nanolab version 13.8, quantumwise a/s (2015).
[44] M. Brandbyge, J.-L. Mozos, P. Ordejón, J. Taylor, and K. Stokbro, Phys. Rev. B **65**, 165401 (2002).
[45] J. M. Soler, E. Artacho, J. D. Gale, A. García, J. Junquera, P. Ordejón, and D. Sánchez-Portal, J. Phys. Condens. Matter **14**, 2745 (2002).
[46] B. Sa, Y.-L. Li, J. Qi, R. Ahuja, and Z. Sun, J. Phys. Chem. C **118**, 26560 (2014).
[47] V. Tran, R. Soklaski, Y. Liang, and L. Yang, Phys. Rev. B **89**, 235319 (2014).
[48] H. Guo, N. Lu, J. Dai, X. Wu, and X. C. Zeng, J. Phys. Chem. **118**, 14051 (2014).
[49] S. Lee, *Sir Rudolf Peierls: Selected Private and Scientific Correspondence*, Vol. 1 (World Scientific, 2007).
[50] H. Ren, Q.-X. Li, Y. Luo, and J. Yang, Appl. Phys. Lett. **94**, 173110 (2009).
[51] S. Chakrabarty, A. H. M. A. Wasey, R. Thapa, and G. P. Das, AIP Adv. **5**, 087163 (2015).
[52] Y. Du, H. Liu, Y. Deng, and P. D. Ye, ACS Nano **8**, 10035 (2014).
[53] D. J. Perello, S. H. Chae, S. Song, and Y. H. Lee, Nat. Commun. **6**, 7809 (2015).